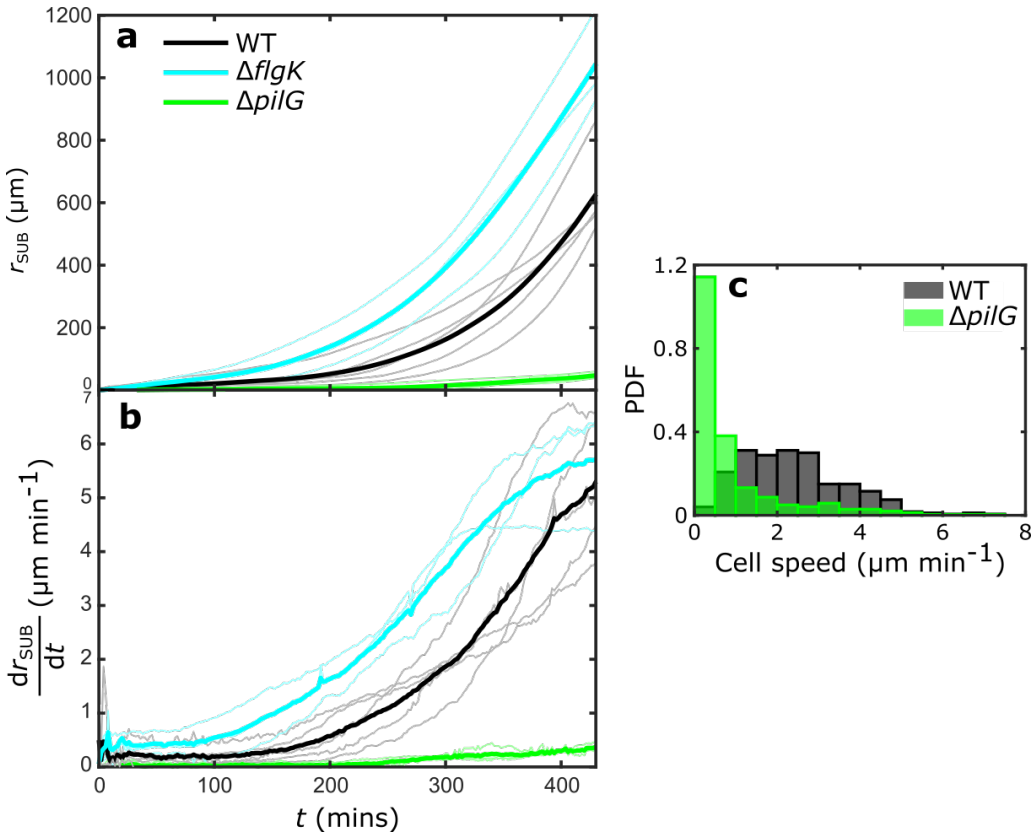

Extended Data Fig. 1 | In the subsurface environment, colonies composed of cells lacking flagella expand faster than those of WT cells, while pili-based chemotaxis mutants display little, if any, motility. a, **b**, Measurements of the colony radius, r_{SUB}, and colony expansion rate, $\frac{dr_{\mathrm{SUB}}}{dt}$, for the wild-type (WT, black, n = 5), a non-flagellated mutant (Δ*flgK*, cyan, n = 3) and a mutant previously shown to be incapable of generating pilus-based chemotaxis in microfluidic devices[18] (Δ*pilG*, green, n = 3). Thick lines indicate the mean of n different colonies. Comparison of Δ*flgK* and WT data indicate that flagella actually hinder colony expansion. We speculate this is because flagella actively stick to surfaces[18], increasing the cells' resistance to movement. **c**, Single-cell speed distributions of WT (n = 347) and Δ*pilG* cells (n = 483) when mixed together at low cell density. The speed of solitary Δ*pilG* cells was significantly smaller than that of solitary WT cells ($p < 10^{-68}$, Mann-Whitney U test), demonstrating that the slow expansion of Δ*pilG* colonies is caused by a more general defect in their motility, rather than a lack of chemotaxis. Δ*pilG* cells express few pili[17], which likely impedes their ability to move in high friction environments like those found in agar-based subsurface assays.

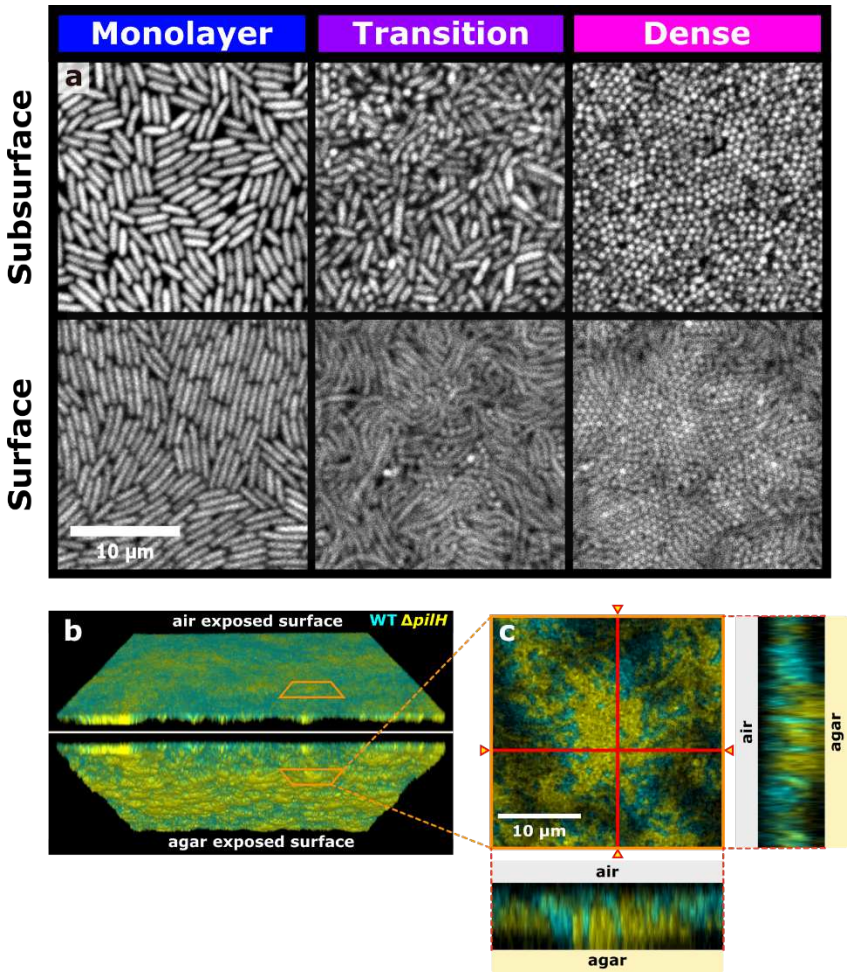

Extended Data Fig. 2 | Cells have similar orientations in both subsurface and surficial colonies. a, Surficial and subsurface colonies of YFP labelled WT cells were grown for 24 h at room temperature and then imaged using confocal microscopy (Methods). Both subsurficial (upper row) and surficial (lower row) colonies have a "monolayer" of cells lying flat against the surface at their periphery, a "dense" region where most cells are vertically standing up on end at their center, and a "transition" region where some cells are standing up between the colony edge and center (Fig. 1b-d). We note that subsurface colony images shown here are the same as those presented in Fig. 1d, but are reproduced here to facilitate direct comparison. **b**, Volumetric projections of a confocal image of a surficial colony inoculated with equal fractions of WT-CFP and Δ*pilH*-YFP cells. In the upper projection, the three-dimensional image is tilted to show the upper air-exposed surface of the colony, while in the lower projection the image is tilted in the opposite direction to show the side of the colony facing the agar. As the thickness of surficial colonies increases over time, we imaged the colony 16 h after inoculation while it was still sufficiently thin to visualise its entire depth using confocal microscopy. Each edge of the imaged region is 170 µm long. A zoomed-in view of the region within the orange boxes (**c**) shows that nearly all of the vertically oriented cells protruding into the agar below are Δ*pilH*-YFP cells, while WT-CFP cells tend to remain closer to the air-exposed surface. Orthogonal views show cross sections through the colony at the locations marked by the red lines. These images demonstrate that Δ*pilH* tends to form structures in surficial colonies similar to those observed in subsurface colonies (Fig. 4f).

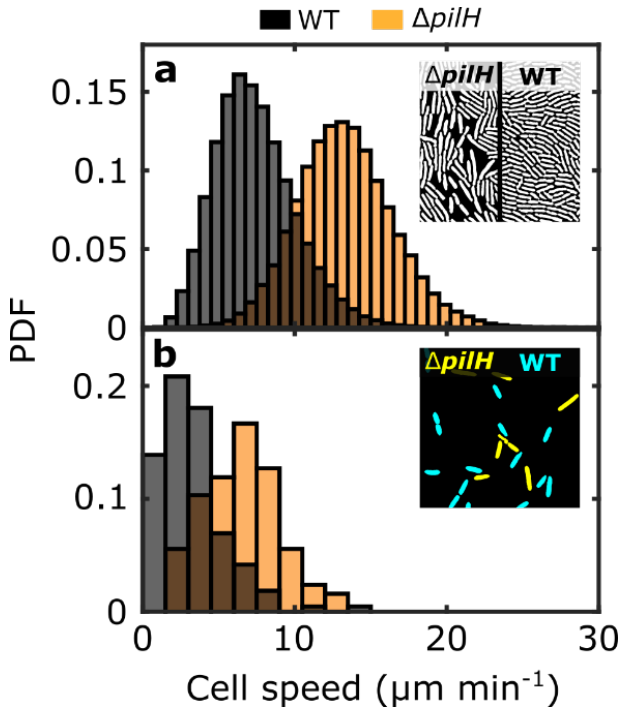

Extended Data Fig. 3 | Δ*pilH* cells move faster than WT cells. Cells in the monolayer of Δ*pilH* colonies move faster than those in WT colonies (Fig. 1e, reproduced in **a**). However, Δ*pilH* monolayers are also observed to have a smaller packing fraction than WT monolayers (**a**, inset). To test if the variation in cell density could confound our analyses, we also performed a separate experiment in which Δ*pilH* and WT cells were mixed together at low density. Separate fluorescent markers were used to distinguish strains (**b**, inset). This confirmed that Δ*pilH* cells move more quickly than WT cells when the two are at equal density ($p < 10^{-17}$, Mann-Whitney *U* test). All experiments shown were performed using the subsurface assay.

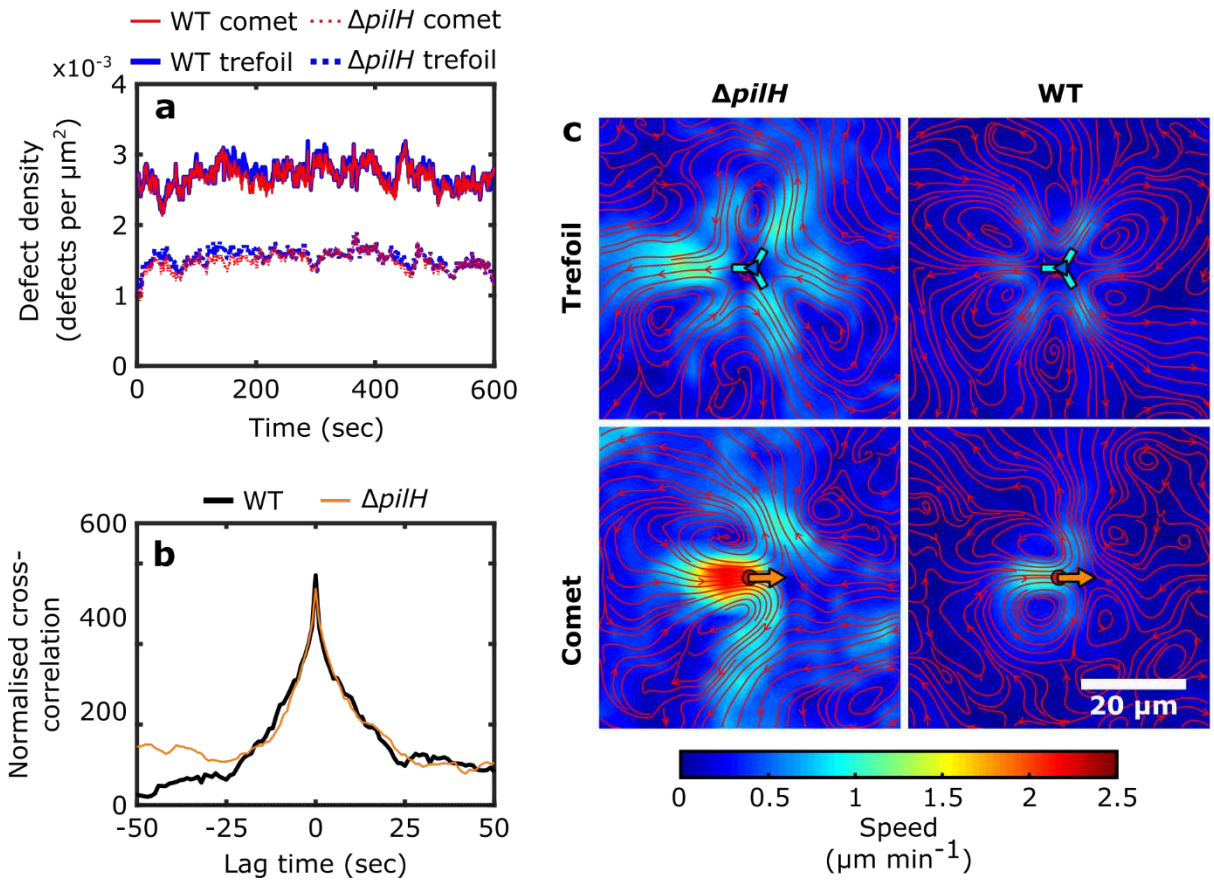

Extended Data Fig. 4 | Automated analysis of defects reveals differences between the collective motility of WT and Δ*pilH* monolayers. a, We used automated defect detection to count the number of comets/trefoils in monolayers of both genotypes and normalized these by the area of the field of view (Methods). Averaging over time, we found that WT monolayers contain 79% more defects than Δ*pilH* monolayers. Fluctuations in the numbers of comets and trefoils closely follow one another, as predicted by nematic theory which requires that the total topological charge of the system must remain fixed[9]. **b**, This relationship was quantified further by calculating the normalized cross-correlation between comet and trefoil density. The maximum cross-correlation occurs at a lag time of zero for both strains, indicating that comet/trefoil pairs are created and annihilated instantaneously. This matches predictions made by previous SPR simulations[50]. **c**, Timeseries of Δ*pilH* and WT monolayers were processed to obtain measurements of the average flow of cells around comets and trefoils as for Fig. 3d. While the same characteristic flow structures were observed in both strains, we observed that the magnitude of the flow velocity was larger for the Δ*pilH* monolayer. This is consistent with Δ*pilH* monolayers having a larger activity than WT monolayers[10].

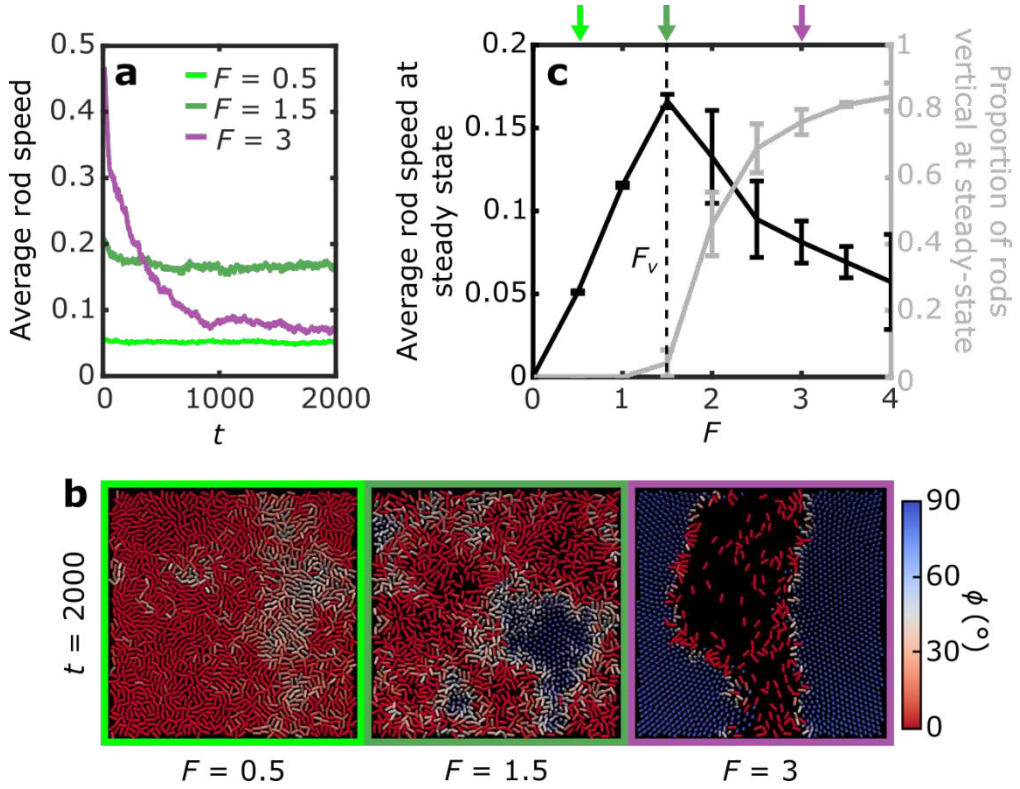

Extended Data Fig. 5 | Rods that propel themselves with larger forces are more likely to become vertically oriented, which disrupts collective movement. a, Measurements of the average rod speed as a function of time in three different simulations, each of which contains a uniform population of $N = 1600$ rods with an aspect ratio of $a = 4$ and a self-propulsive force, F. Although rods with $F = 1.5$ collectively move faster than rods with $F = 0.5$, increasing the propulsive force to $F = 3$ causes collective speed to sharply decline over time. **b**, Snapshots of simulations shown in a at steady state. Rods are color-coded by their orientation with respect to the surface, ϕ, such that rods lying flat against the surface are shown in red, while those orthogonal to the surface are shown in blue. Rods with larger F are more likely to stand on end, disrupting their capacity to move. **c**, We then performed independent simulations for different values of F and plotted the average rod speed and proportion of rods oriented orthogonal to the surface at steady-state (Methods). This shows that the mean speed of the collective peaks at intermediate F, with larger values of F causing rods to become vertically oriented. We denote the force that generates the maximum mean rod speed as F_v. Values of F for simulations shown in a and b are denoted by coloured arrows. Our results show that out of plane cell rotation places an upper limit on how much propulsive force can be exerted within collectives. Lines and error bars show the mean and standard deviation of three simulations with different (random) initial conditions.

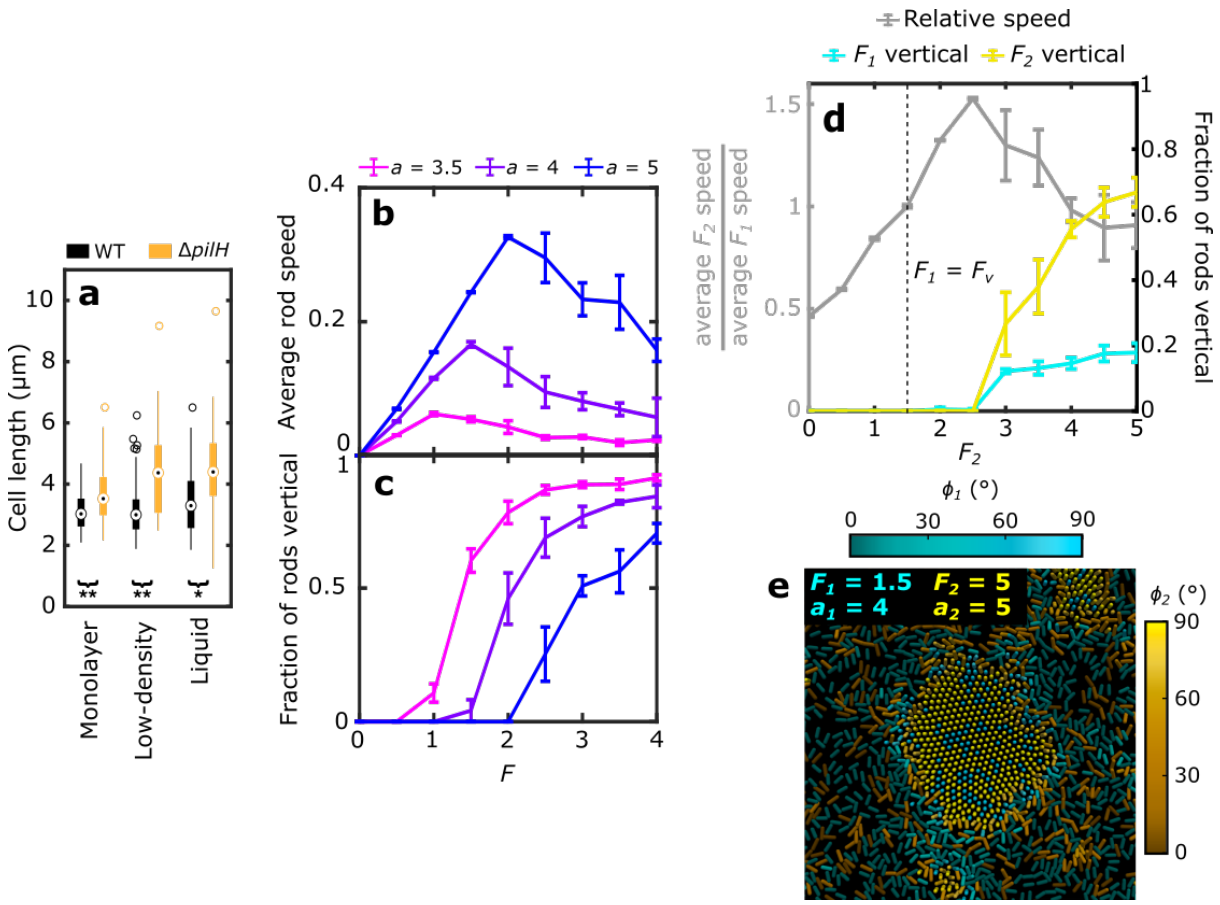

Extended Data Fig. 6 | Δ*pilH* cells are longer than WT cells, which stabilizes them against verticalization but increases their representation in rosettes when mixed with a shorter genotype. a, Boxplots of lengths of WT (black) and Δ*pilH* (orange) cells mixed together in a high-density subsurface colony ("Monolayer", WT n = 223, Δ*pilH* n = 218), a low-density subsurface colony ("Low-density", WT n = 114, Δ*pilH* n = 84), and in liquid culture at exponential phase ("Liquid", WT n = 60, Δ*pilH* n = 34) (Methods). The Δ*pilH* cells were significantly longer than WT cells in all three environments (* = $p < 10^{-3}$, ** = $p < 10^{-10}$, Mann-Whitney U test). Boxplots indicate the median (central white rings), interquartile range (box limits), 1.5x interquartile range (whiskers) and outliers (individual circles). **b**, Average rod speed at steady-state in 3D SPR monolayer simulations for rods with different propulsive forces, F, and rod aspect ratio, a. All rods in a given simulation have identical parameters. **c**, Proportion of rods oriented vertically at the end of simulations shown in b. **d**, Steady state velocity and verticalization measurements for simulations in which a "mutant" population of rods that are propelled by a variable force F_2 and with a fixed aspect ratio $a_2 = 5$ interacts with a "wild-type" population with $F_1 = F_v = 1.5$ (fixed), $a_1 = 4$ (fixed). These simulations are similar to the ones shown in Fig. 4b, except the two populations of rods also have different aspect ratios. Error bars in b-d indicate the standard deviation of three separate simulations, each with a different random initial configuration. **e**, A rosette spontaneously generated in co-culture simulation with parameters $F_1 = F_v = 1.5$, $a_1 = 4$, $F_2 = 5$ and $a_2 = 5$ illustrates how the longer length of the mutant enhances its representation in rosettes (compare with Fig. 4c and see Supplementary Notes).

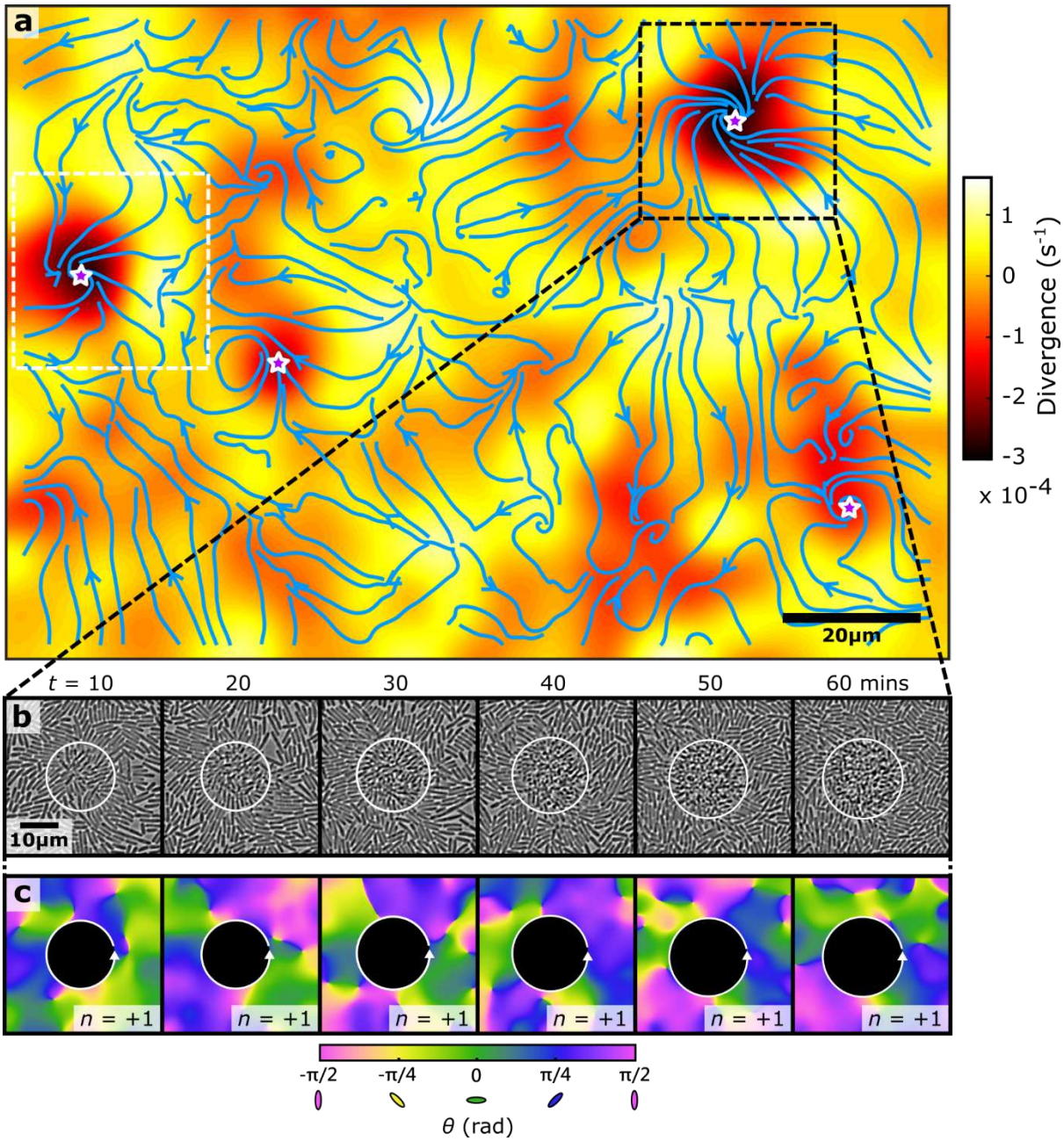

Extended Data Fig. 7 | Rosettes drive convergent flow in a mixed WT/Δ*pilH* subsurface colony and have a topological charge of +1. a, We used particle image velocimetry (PIV) to quantify collective cell movement in a monolayer of cells over a period of 60 mins. The divergence and streamlines of the temporally averaged velocity field reveal that cells locally accumulate (indicated by negative divergence) at rosettes (purple stars). **b**, A timeseries of brightfield images during rosette formation illustrates this process (also shown in Fig. 4d-f and the first part of Supplementary Video 9), with increasing numbers of cells becoming verticalized and trapped within the boundary of the rosette core (white circles) over time. By calculating the director field of these images (Methods), we can calculate the topological charge n around the core of the rosette (white circular arrows). At all timepoints, the charge of the rosette is equal to +1. In a, the region shown in the second part of Supplementary Video 9 is indicated with a white dashed box.

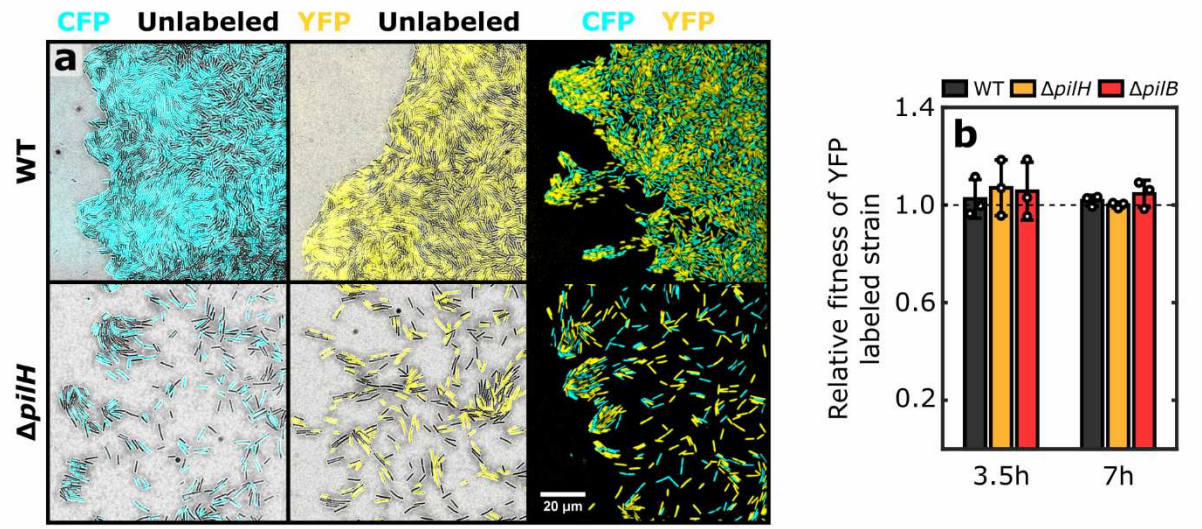

Extended Data Fig. 8 | Neither labelling cells with constitutively expressed fluorescent proteins nor the deletion of *pilH* or *pilB* has an appreciable impact on the intrinsic growth rate of cells. a, The leading edge of six different subsurface colonies inoculated with equal fractions of CFP labelled and unlabelled strains (left), YFP labelled and unlabelled strains (middle), and CFP labelled and YFP labelled strains (right) after 16 h of incubation at room temperature. WT and Δ*pilH* colonies are shown on the upper and lower rows respectively. In all six colonies, near equal proportions of each cell type are present at the colony's leading edge indicating that expression of a fluorescent label has a negligible impact on each strain's competitive ability. Unlabelled strains are imaged using brightfield and appear grey. **b**, Relative fitness of three YFP labelled test strains (WT, Δ*pilH* and Δ*pilB*) compared to a CFP labelled WT reference strain mixed together in liquid culture. The relative fitness of each test strain was not significantly different from 1 at either 3.5 or 7 h post-inoculation ($p > 0.05$, one sample t-test, $n = 3$, Methods). Error bars indicate standard deviation of 3 replicates.

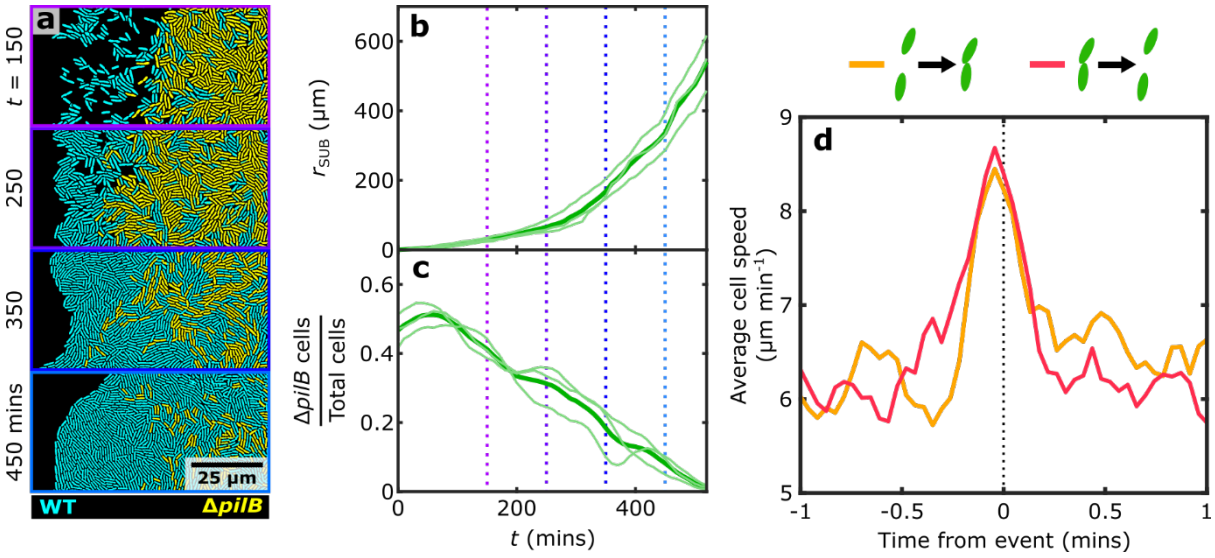

Extended Data Fig. 9 | Differences in motility, rather than differences in cell-cell adhesion, drive changes in strain composition at the front of subsurface colonies. a, Images of the leading edge of a subsurface colony initialised with equal numbers of Δ*pilB*-YFP and WT-CFP cells at 150, 250, 350 and 450 minutes after the start of imaging, processed as shown in Supplementary Fig. 1i. During colony expansion (**b**) a small number of non-piliated Δ*pilB* cells were observed to be dragged along by motile WT cells. However, over time the number of Δ*pilB* cells near the edge of the colony gradually declined (**c**). These results are in stark contrast to those of equivalent *Neisseria gonorrhea* colonies, where non-piliated cells are pushed to the colony edge due to decreased intercellular adhesion[24]. Thick lines in **b** and **c** indicate the mean of three separate colonies. We note that *N. gonorrhoeae* cells are spherical, a shape which is predicted to produce a jammed state in dense collectives[15]. In contrast, steric interactions between rod-shaped *P. aeruginosa* cells produce local nematic alignment, permitting collective motility and so explaining why motility is dominant over adhesion in this system. **d**, Δ*pilH* cells are hyperpilated, which has been shown to increase cell-cell adhesion in other systems[24,25]. We tested for the importance of this effect by measuring the mean speed of previously solitary Δ*pilH* cells as they came into contact with one another (orange line, $n = 41$) and the mean speed of Δ*pilH* cells already in contact with one another as they moved apart (red, $n = 47$). If cells actively adhered to each other, we would expect them to slow down after contacting one another and increase their speed after moving away from one another (Supplementary Notes). We find that cell speed peaks at $t = 0$, which corresponds to the time point at which cells either make or break contact. However, in both cases we observed that there was no appreciable change in cell speed before or after either event, indicating that Δ*pilH* cells do not appreciably adhere to each other.

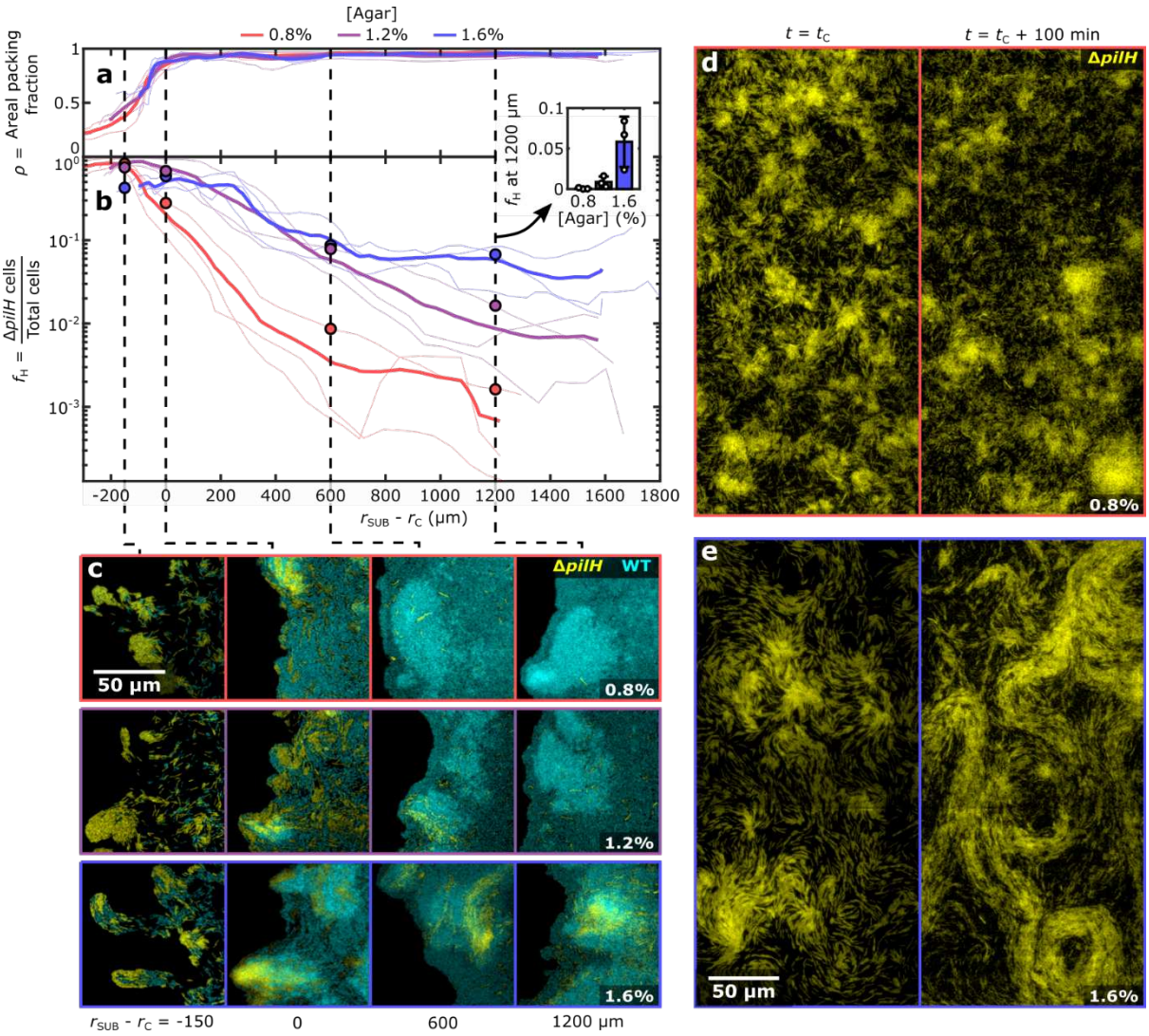

Extended Data Fig. 10 | Stiffer agar suppresses rosettes, increasing the fraction of Δ*pilH* cells at the front of mixed WT/Δ*pilH* colonies as they expand. a, Subsurface colonies prepared with 0.8% (red), 1.2% (purple) and 1.6% (blue) agar were inoculated with equal fractions of WT-CFP and Δ*pilH*-YFP cells. Cells in colonies prepared with 1.6% agar are predicted to experience an approximately four-fold larger stabilizing torque compared to those with 0.8% agar, which acts to resist the formation of vertically oriented rosettes (Supplementary Notes). Here, we plot the packing fraction, ρ, at the front of colonies as they expand across the surface, aligning each by the radius at which the front becomes fully packed with cells, or confluent (r_C). This collapses data from all colonies onto a single curve and allows us to control for variation across replicates (Supplementary Notes). **b**, Measurements of the Δ*pilH* to total cell fraction, f_H, at the colony front shows that stiffer agar allows Δ*pilH* cells to migrate greater distances. The inset shows f_H at $r_{SUB} - r_C = 1200$ µm, the final position for which data is available for all replicates. We find that f_H is positively correlated with agar concentration at this position ($p < 0.005$, $n = 9$, Spearman's rank correlation test), demonstrating that stiffer substrates allow Δ*pilH* cells to migrate further when competed against WT cells. **c**, The increased persistence of Δ*pilH* cells can readily be observed in representative images of the front of 0.8% (top), 1.2% (middle) and 1.6% agar (bottom) colonies. Dashed lines indicate the corresponding positions in **b**. **d**, **e**, Images of the region

behind the front at the confluency time t_C and t_C + 100 min in colonies prepared with 0.8% (**d**) and 1.6% (**e**) agar. With 0.8% agar, Δ*pilH* cells form numerous discrete, tightly-packed rosettes. With 1.6% agar, Δ*pilH* cells still form aggregations but remain horizontally oriented, allowing them to escape and form plume-like patterns. To improve clarity, only YFP-expressing Δ*pilH* cells are shown in **d** and **e**. Thick lines in **a**, **b** show the mean of three separate colonies.